

1 **Climatology and annual cycle of global ocean dissolved oxygen represented by multiple**
2 **observational gridded products**

3 Juan Du¹, Lijing Cheng², Takamitsu Ito³, Hernan E. Garcia⁴, Zhankun Wang⁴, Jonathan D.
4 Sharp^{5,6}, Christopher J. Roach⁷, Shoshiro Minobe⁸, Yuntao Zhou⁹, Bin Lu¹⁰, Gian Giacomo
5 Navarra¹¹, Seth M Bushinsky¹²
6

7 ¹International Center for Climate and Environment Sciences, Institute of Atmospheric
8 Physics, Chinese Academy of Sciences, Beijing, China.

9 ²State Key Laboratory of Earth System Numerical Modeling and Application, Institute of
10 Atmospheric Physics, Chinese Academy of Sciences, Beijing, China.

11 ³School of Earth and Atmospheric Sciences, Georgia Institute of Technology, Atlanta,
12 Georgia, USA.

13 ⁴NOAA, National Centers for Environmental Information, Silver Spring, Maryland, USA.

14 ⁵Cooperative Institute for Climate, Ocean, and Ecosystem Studies, University of Washington,
15 Seattle, Washington, USA.

16 ⁶Pacific Marine Environmental Laboratory, National Oceanic and Atmospheric
17 Administration, Seattle, Washington, USA.

18 ⁷Institute for Marine and Antarctic Studies, University of Tasmania, Hobart, Australia.

19 ⁸Department of Earth and Planetary Sciences, Faculty of Science, Hokkaido University,
20 Sapporo, Japan.

21 ⁹School of Oceanography, Shanghai Jiao Tong University, Shanghai, China.

22 ¹⁰School of Information Science and Electronic Engineering, Shanghai Jiao Tong University,
23 Shanghai, China.

24 ¹¹Department of Geosciences, Princeton University, Princeton, New Jersey, USA.

25 ¹²Department of Oceanography, School of Ocean and Earth Science and Technology,
26 University of Hawaii at Manoa, Honolulu, Hawaii, USA.

27
28 **Corresponding author:** Juan Du (dujuan10@mail.iap.ac.cn)
29

30 **Abstract:**

31 Ocean dissolved oxygen (O₂) is an essential climate variable crucial for sustaining the marine
32 life; thus, changes of O₂ at various spatiotemporal scales should be quantified and
33 understood. Here, we study the climatology and annual cycle of O₂ at regional to global
34 scales using eight available gridded observational products. These datasets are generated by
35 different groups using different primary data selection, quality control, bias correction, and
36 interpolation methods, including statistical and machine-learning-based mapping methods. A
37 common set of metrics was collaboratively developed by the community of the Gridded
38 Observational Dataset Intercomparison Project-Dissolved Oxygen (GODIP-DO) to facilitate
39 the inter-comparison. We find that global mean O₂ profiles are consistent among all products
40 ($\pm 3 \mu\text{mol kg}^{-1}$), with the well-established decrease from high surface values to a minimum
41 ~ 1000 meters, and subsequent increase to higher O₂ at depth, although local differences could
42 reach $\pm 25 \mu\text{mol kg}^{-1}$ (0-1000 m). The hemispheric O₂ annual cycle correlates strongly with

43 ocean temperature changes, suggesting the key driver of temperature for the O₂ annual cycle.
44 However, there is substantial variation in the global mean 0-100 m O₂ annual cycle, the
45 magnitude ranges from -1 to 0.8 μmol kg⁻¹, with a standard deviation of the datasets of ~0.3
46 μmol kg⁻¹. Average oxygen minimum zones (OMZ) volume among the products is 80.92 ×
47 10⁶ km³ (±1.95 %) for a 60 μmol kg⁻¹ threshold and 152.00 × 10⁶ km³ (±1.72 %) for a 90
48 μmol kg⁻¹ threshold. Our results help to depict and understand the spread among the available
49 O₂ gridded datasets.

50

51 **1 Introduction**

52 Anthropogenic climate change drives ocean warming, increases stratification, and alters
53 ocean circulation (Bindoff et al. 2019). These changes lead to the loss of ocean dissolved
54 oxygen (O₂), namely deoxygenation, because of the changes in the O₂ solubility, ventilation,
55 and deep ocean respiration (Keeling et al., 2010; Schmidtko et al., 2017; Breitburg et al.,
56 2018; Oschlies et al., 2018; Garcia-Soto et al., 2021). Deoxygenation occurred in most open
57 ocean regions during the mid-20th to early 21st centuries, such as the Mediterranean Sea,
58 tropical oxygen minimum zones (OMZ), and the North Atlantic Subtropical Gyre (Tan et al.,
59 2026), influencing marine ecosystems through resulting biogeochemical feedbacks such as
60 ocean productivity, nutrient cycling, carbon cycling, marine habitat, etc (Levin, 2018;
61 Bindoff et al., 2019). Given its importance, studying O₂ changes at various spatiotemporal
62 scales becomes critical.

63 Observations and model simulations document a robust decline of the global O₂
64 inventory, which is a grand challenge for the accurate assessment of deoxygenation (Ito et al.,
65 2017; Schmidtko et al., 2017; Breitburg et al., 2018). For trends, current assessments such as
66 the Intergovernmental Panel on Climate Change (IPCC) Special Report on the Ocean and
67 Cryosphere in a Changing Climate (SROCC) indicates that the open ocean is losing O₂
68 overall with a decadal variability of 0.3-2 % since the 1960s over all ocean depths and of 0.5–
69 3.3 % between 1970 and 2010 from the ocean surface to 1000 m, with an expansion of OMZ
70 by 3–8 % (Bindoff et al., 2019; Gulev et al., 2021; Zhou et al., 2022). In addition, a recent
71 observational-based assessment by Tan et al. (2026) shows that significant signal emergence
72 of long-term O₂ trends (both deoxygenation and oxygenation) can now be detected across
73 global ocean in a large-scale and deep-reaching pattern since the 1990s, although the regional
74 data uncertainty still needs to be taken into account. These studies reveal substantial
75 uncertainty in quantifying the open ocean O₂ trends, however, there is no dedicated study

76 assessing the available products on O₂ climatology and its annual cycle, which is the key
77 focus of the present study.

78 The differences among different O₂ products may arise from the instruments/platforms
79 used to obtain O₂ profiles and the data processing techniques including quality control
80 processes, bias correction approaches, vertical interpolation methods, mapping methods
81 (horizontal interpolation), land-ocean masks, and so on. Since the late 19th century,
82 oceanographers have measured ocean O₂ using many observing systems with varying
83 sampling resolutions. The very first observing system includes the chemical titration method
84 developed by Winkler (Ocean Station Data, OSD), which restricted the O₂ observations
85 derived from water samples to several depth levels. Electrochemical and optical sensors for
86 measuring O₂ became prevalent in the 1960s-70s and are now widely used to make
87 continuous measurements on platforms such as the CTD (Conductivity-Temperature-Depth)
88 profilers. Biogeochemical Argo profiling floats (BGC-Argo) have provided increasing ocean
89 O₂ observation profiles since the early 2000s, and underwater gliders (GLD) and moorings
90 are especially useful for regional oceanography (Gregoire et al., 2021; Gourteski et al., 2024).
91 The Winkler data are labour intensive with lower sampling resolution, whereas sensor-based
92 measurements have better spatiotemporal resolution, and the proliferation of the BGC-Argo
93 program has dramatically increased O₂ observations.

94 With the ocean O₂ observations collected using different observing systems, there have
95 been several quality controlled global ocean O₂ observation datasets from different research
96 organizations/groups such as the National Centers for Environmental Information (NCEI) of
97 the National Oceanic and Atmospheric Administration (NOAA) (Garcia et al., 2024; Garcia
98 et al., 2018; Boyer et al., 2018), Shanghai Jiao Tong University (SJTU, Zhou et al., 2022) and
99 the Institute of Atmospheric Physics (IAP) Chinese Academy of Sciences (Gourteski et al.,
100 2024). These quality controlled observations are then used to construct gridded O₂ data
101 products by filling data gaps with a mapping method where direct observations were not
102 available. The available mapping methods include objective analysis (Garcia et al., 2024),
103 ensemble optimal interpolation with dynamic ensemble (Cheng et al., 2024; Cheng et al.,
104 2017; Cheng and Zhu, 2016), Data Interpolating Variational Analysis (DIVA; Roach and
105 Bindoff, 2023), machine learning techniques (Sharp et al., 2023; Ito et al., 2024; Huang et al.,
106 2023; Liu et al., 2025), and geostatistical regression (Zhou et al., 2022).

107 All the previously mentioned instrumental data have measurement errors and biases,
108 and the data processing techniques are imperfect, leading to uncertainty in representing the
109 O₂ climatological mean state and its annual variation. A systematic multi-product

110 intercomparison at regional to global scales could serve as the primary tool to assess the
111 robustness of our observational understanding and to quantify the spread in current
112 climatological representations. The spread among different datasets includes all uncertainty
113 factors and is different from the recent single-factor assessment of Ito et al. (2025) who
114 focused solely on mapping methods. In particular, we employed eight ocean O₂ climatology
115 products, covering statistical and machine-learning-based mapping methods whereas Ito et al.
116 (2025) included statistical mapping methods only. Our analysis includes the gridded O₂
117 dataset from IAP (Gourteski et al., 2024), World Ocean Atlas 2023 (hereafter, WOA23; Garcia
118 et al., 2024) and World Ocean Atlas 2018 (hereafter, WOA18; Garcia et al., 2018; Boyer et
119 al., 2018) by NCEI, a machine-learning-based data product by Sharp et al. (2023) (Gridded
120 Ocean Biogeochemistry from Artificial Intelligence, hereafter, GOBAI; Sharp et al., 2023),
121 two data products based on DIVA by Roach and Bindoff (2023) (hereafter, RB; Roach and
122 Bindoff, 2023) and Global Ocean Data Analysis Project (hereafter, GLODAP; Lauvset et al.,
123 2016), a geostatistical gridded O₂ dataset from SJTU (Zhou et al., 2022), and a machine-
124 learning-based data product (hereafter, Jingwei; Lu et al., 2024).

125 The rest of the paper is organized as follows. The gridded datasets and methods
126 employed in the study are presented in Section 2. In Section 3, the results of depicting the
127 characteristics and assessing the spread of O₂ climatology and annual cycle for different
128 products are introduced. The analysis related to OMZ distribution is also presented in Section
129 3. The results of the study are summarized and discussed in Section 4.

130

131 **2 Datasets description**

132 We used eight O₂ gridded products (IAP, WOA23, WOA18, GOBAI, RB, GLODAP,
133 SJTU, and Jingwei) that are different in many aspects including the instruments to get raw O₂
134 profiles and also the data processing techniques, such as quality control and bias correction
135 approaches, vertical interpolation methods, mapping methods, land-ocean masks, and so on
136 (Table 1).

137 The observations used by IAP, WOA23, WOA18, RB, SJTU, and Jingwei are mainly
138 from WOD (World Ocean Database, Boyer et al., 2018; Mishonov et al., 2024) and BGC-
139 Argo. Observations from GLODAP are also used in GOBAI product. The IAP, WOA23,
140 WOA18, and GOBAI datasets include monthly climatology, and the remaining four data
141 products (RB, GLODAP, SJTU, and Jingwei) only provide the annual mean climatology. So,
142 analyses related to the annual variation of the global ocean O₂ and the annual cycle are
143 restricted to the four datasets with monthly climatology (IAP, WOA23, WOA18, and

144 GOBAI). The gridded data products of IAP, WOA23, WOA18, RB, GLODAP, and Jingwei
 145 reach the ocean bottom of about 5500 m/6000 m. GOBAI and SJTU only cover the top 2000
 146 m. The horizontal resolution of the data product of RB and SJTU is $0.5^\circ \times 0.5^\circ$ and $2^\circ \times 2^\circ$,
 147 respectively, and all the other six products are at a resolution of $1^\circ \times 1^\circ$. The horizontal space
 148 coverages of all the datasets are also slightly different. The space coverage of the GOBAI
 149 data is limited by the distribution of the temperature and salinity data product on which it is
 150 based, so GOBAI only covers 64.5° S- 79.5° N of the open ocean (O_2 in the coastal regions
 151 and oceans with complex topography are not reconstructed). The mapping method for
 152 WOA18 and WOA23 is based on objective analysis and that for IAP is the ensemble optimal
 153 interpolation with dynamic-ensemble. GLODAP and RB both adopt the DIVA method to
 154 generate gap-filled fields. SITU develops the geostatistical regression interpolation method.
 155 The feed-forward neural network and the spatio-temporal graph hypernetwork are used for
 156 the machine learning process of the GOBAI and Jingwei data products, respectively (Table
 157 1). To illustrate the spatiotemporal characteristics of the observation profiles, the spatial
 158 distribution and annual number of the three main observation platforms (OSD, CTD, BGC-
 159 Argo) for 1960-2024 are shown in Fig. 1.

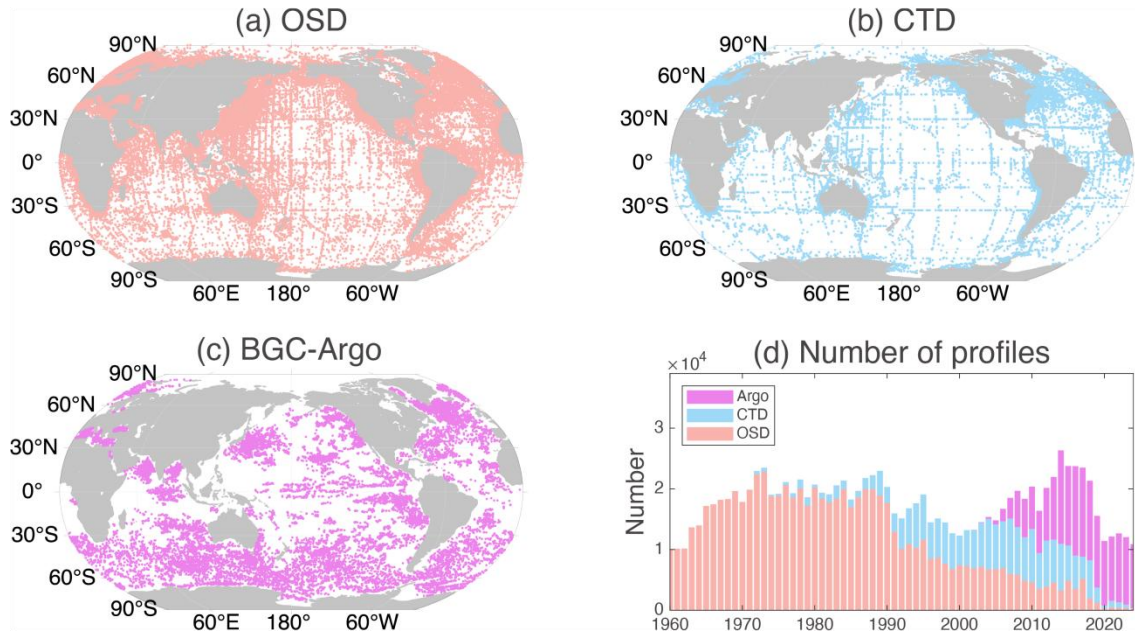
160

161 **Table 1** Global ocean O_2 gridded datasets employed in the comprehensive inter-comparison
 162 of the climatology (EnOI-DE: ensemble optimal interpolation with dynamic-ensemble; OA:
 163 objective analysis; ML: machine learning; GR: geostatistical regression).

O_2 Datasets	Mapping	Quality Control	Time Period	Resolution	Depth/Layers	Observations
IAP Gourteski et al. (2024)	EnOI-DE	IAP	1960-2022	$1^\circ \times 1^\circ$	6000 m/119	OSD, CTD, BGC-Argo
WOA23 Garcia et al. (2024)	OA	NCEI	1965-2022	$1^\circ \times 1^\circ$	5500 m/102	OSD, CTD, BGC-Argo
WOA18 Boyer et al. (2018)	OA	NCEI	1960-2017	$1^\circ \times 1^\circ$	5500 m/102	OSD
GOBAI Sharp et al. (2023)	ML	GLODAP, BGC-Argo	2004-2024	$1^\circ \times 1^\circ$	1975 m/58	OSD, BGC-Argo

RB Roach and Bindoff (2023)	DIVA	NCEI	1960-2017	$0.5^\circ \times 0.5^\circ$	6100 m/108	OSD, CTD
GLODAPv2 Lauvset et al. (2016)	DIVA	GLODAP	1972-2013	$1^\circ \times 1^\circ$	5500 m/33	OSD
SJTU Zhou et al. (2022)	GR	NCEI, SJTU	1960-2019	$2^\circ \times 2^\circ$	2000 m/61	OSD, CTD, BGC-Argo, GLD
Jingwei Lu et al. (2024)	ML	NCEI	1960-2023	$1^\circ \times 1^\circ$	5500 m/33	OSD, CTD, BGC-Argo

164



165

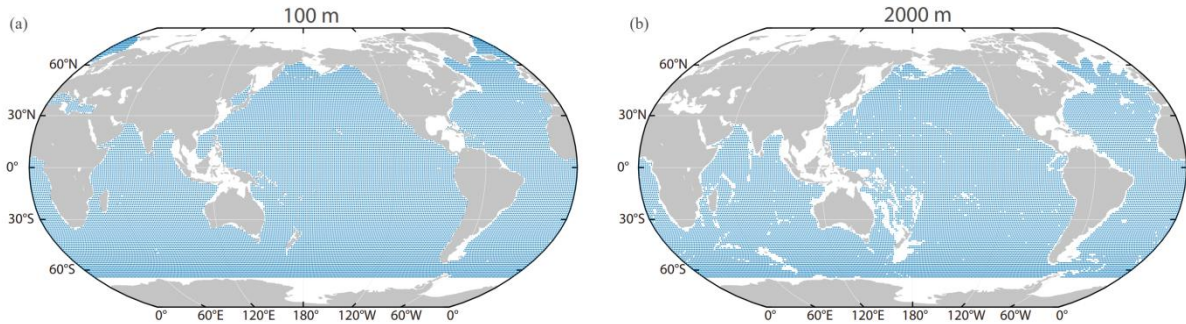
166 **Figure 1** Spatial distribution (a: OSD, b: CTD, c: BGC-Argo) and annual number (d) of
 167 observation profiles.

168

169 This study used a common ocean mask, which is defined as ocean grid points with all
 170 data products available. The common land-ocean masks for the layers of 100 m and 2000 m
 171 are presented in Fig. 2 and the common masks for the other layers (1000 m, 3000 m, 4000 m,
 172 and 5000 m) are available in Fig. S1. This will be a uniform comparison and remove the
 173 impacts of different data coverage on the results. The datasets of RB and SJTU were

174 interpolated to a common $1^\circ \times 1^\circ$ resolution as all the other datasets to facilitate the
175 comparison, but the interpolation has a negligible impact on the results presented in this work
176 (less than 0.01% for the global mean O_2).

177



178

179 **Figure 2** Grid point distribution of the common land-ocean mask for the layers of 100 m (a)
180 and 2000 m (b).

181

182 **3 Results**

183 **3.1 Global mean O_2**

184 The global area-weighted mean O_2 profile is first presented in Fig. 3a, showing a well-
185 established vertical structure and a good consistency among all products. O_2 is higher near
186 the surface than in the deeper ocean because of the gas exchange with the atmosphere and
187 photosynthesis. The O_2 reaches the lowest value at ~ 1000 m because of the respiration and
188 limited O_2 supply from the surface. The O_2 increases from ~ 1000 m to the deep ocean (~ 5000
189 m) because of the weaker respiration and the intermediate, deep, and bottom water formation
190 that supplies higher O_2 water into the deep layers, where cold, dense surface water sinks, and
191 is then distributed globally by deep ocean currents, slowly losing O_2 along its centuries-long
192 journey (Musun et al., 2023).

193 To better quantify the differences among the datasets, we take the difference between all
194 seven other data products (WOA23, WOA18, GOBAI, RB, GLODAP, SJTU, and Jingwei),
195 and IAP data (Fig. 3e-h). The differences are mostly within $\pm 3 \mu\text{mol kg}^{-1}$ among all the
196 datasets with a common land-ocean mask from ocean surface to 5500 m, except that the
197 differences for SJTU and Jingwei range between $-6 \mu\text{mol kg}^{-1}$ and $5 \mu\text{mol kg}^{-1}$ for the upper
198 200 m. The differences are comparable to the magnitude of O_2 anomaly, whose semi-decadal
199 median is within $\pm 10 \mu\text{mol kg}^{-1}$ within major ocean basins (Schmidt et al., 2017).

200 There is a negative offset between GOBAI and IAP ($\sim -2 \mu\text{mol kg}^{-1}$). The differences
201 between WOA18, RB, and IAP are positive. One possible reason for these differences is that

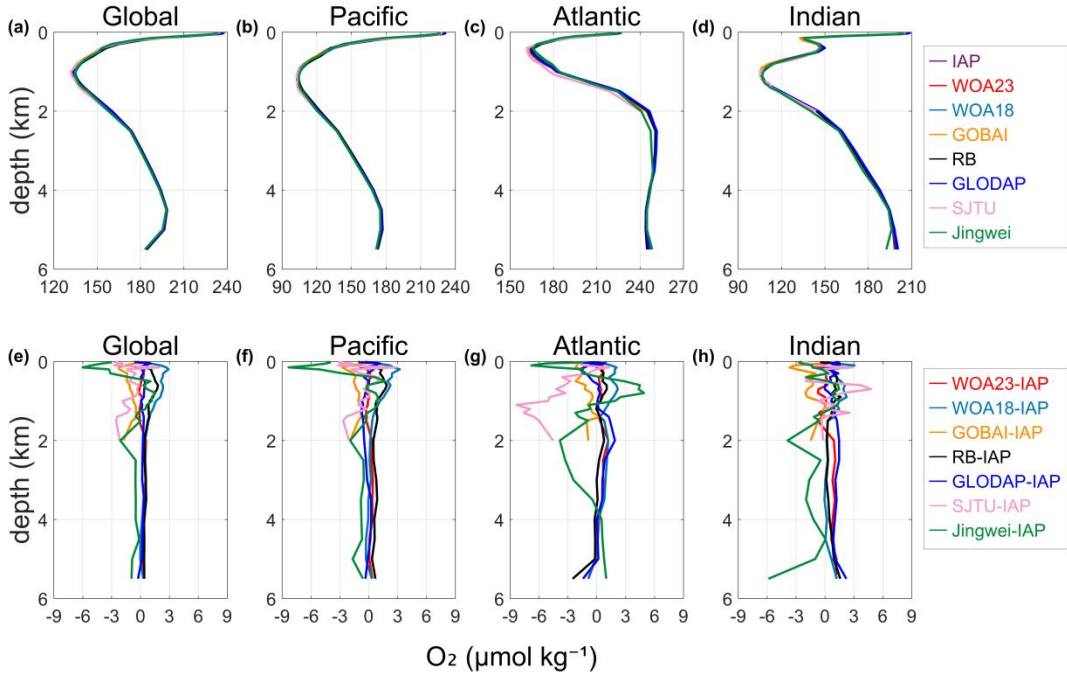
202 different data products construct climatologies using data from different time periods with
203 different resolutions. The SJTU climatology uses CTD, OSD, BGC-Argo, and additional
204 GLD data, then interpolates them at coarser $2^{\circ} \times 2^{\circ}$ resolution. The GOBAI climatology is
205 reflective of a more recent period compared to the other datasets (2004-2024), which might at
206 least partly explain the negative difference between GOBAI and IAP (where data from 1960-
207 2022 are used). Because of the general deoxygenation trend, a “newer” climatology is
208 expected to show less global mean O_2 than an “older” climatology. IAP is close to WOA23 at
209 the upper 2000 m within $1 \mu\text{mol kg}^{-1}$, which is reasonable because both IAP and WOA23
210 used bottle (OSD), CTD, and delayed-mode BGC-Argo data using the same $1^{\circ} \times 1^{\circ}$ data
211 resolution, and they have similar time coverage of data used to generate climatology (IAP,
212 1960-2022, and WOA23, 1965-2022).

213 Below 2000 m, there is an offset between IAP and WOA23: WOA23 O_2 is 0.2-0.6 μmol
214 kg^{-1} higher than IAP. Possible explanations may be the differences in quality control and
215 mapping methods. Another possibility is the ‘jump’ around 2000 m of IAP minus WOA23. It
216 is common to have a discontinuity around 2000 m because of the big differences in data
217 amount and data distributions at upper and deeper layers (observations are concentrated in the
218 upper ocean and most of the BGC-Argo data are in the upper 2000 m). Differences in
219 infilling the empty grid nodes during the mapping procedure may also play a significant role
220 in deep ocean layers where the number of observation data is severely limited. Results of
221 applying different mapping methods to the same in situ datasets suggest that mapping
222 methods may contribute to a difference of less than $\pm 1 \mu\text{mol kg}^{-1}$ for the 0-5500 m area-
223 weighted averaged O_2 (Ito et al., 2025). And using two different quality control processes and
224 the same mapping procedure yields a difference of only $\pm 0.5 \mu\text{mol kg}^{-1}$ (Ito et al., 2025).

225 The mean O_2 profiles and the differences between datasets for major ocean basins
226 (Pacific, Atlantic, Indian) are calculated separately and presented in Fig. 3b-d and Fig. 3f-h.
227 The differences are mostly within $\pm 4 \mu\text{mol kg}^{-1}$ among all the datasets for the Pacific and
228 Indian Oceans, except that the difference for Jingwei ranges between $-8 \mu\text{mol kg}^{-1}$ and 2
229 $\mu\text{mol kg}^{-1}$ for the upper 200 m in the Pacific Ocean (Fig. 3f). The mean O_2 profiles for the
230 Atlantic Ocean show more notable differences compared to other ocean basins (Fig. 3c),
231 including that the mean O_2 profile of SJTU data shows a difference of $-10 \mu\text{mol kg}^{-1}$ to -5
232 $\mu\text{mol kg}^{-1}$ for the depth of 1000-2000 m, while the differences of all the other datasets are
233 constrained to $-5 \mu\text{mol kg}^{-1}$ to $5 \mu\text{mol kg}^{-1}$ from ocean surface to the depth of 5500 m (Fig.
234 3g). For the Atlantic Ocean, the mean O_2 reached the minimum at the depth of ~ 500 m (Fig.
235 3c), which is much shallower than the O_2 minimum layers for the Pacific and Indian Oceans

236 (~1000 m, Fig. 3b, 3d), possibly due to a combined effect of the formation, transport, and
 237 mixing process of the North Atlantic Deep Water (NADW), the ventilation processes such as
 238 Atlantic Meridional Ocean Circulation (AMOC), and so on (Levin, 2018; Koelling et al.,
 239 2022; Musan et al., 2023; Ruhl et al., 2025).

240



241

242 **Figure 3** Area-weighted mean O_2 climatology (a-d) and difference (e-h) relative to the IAP
 243 for the Global, Pacific, Atlantic, and Indian Oceans from ocean surface to 5500 m with a
 244 common ocean mask for different ocean basins in units of $\mu\text{mol kg}^{-1}$. The subplots for O_2
 245 climatology (a-d) use different scales.

246

247 3.2 Zonal mean structure

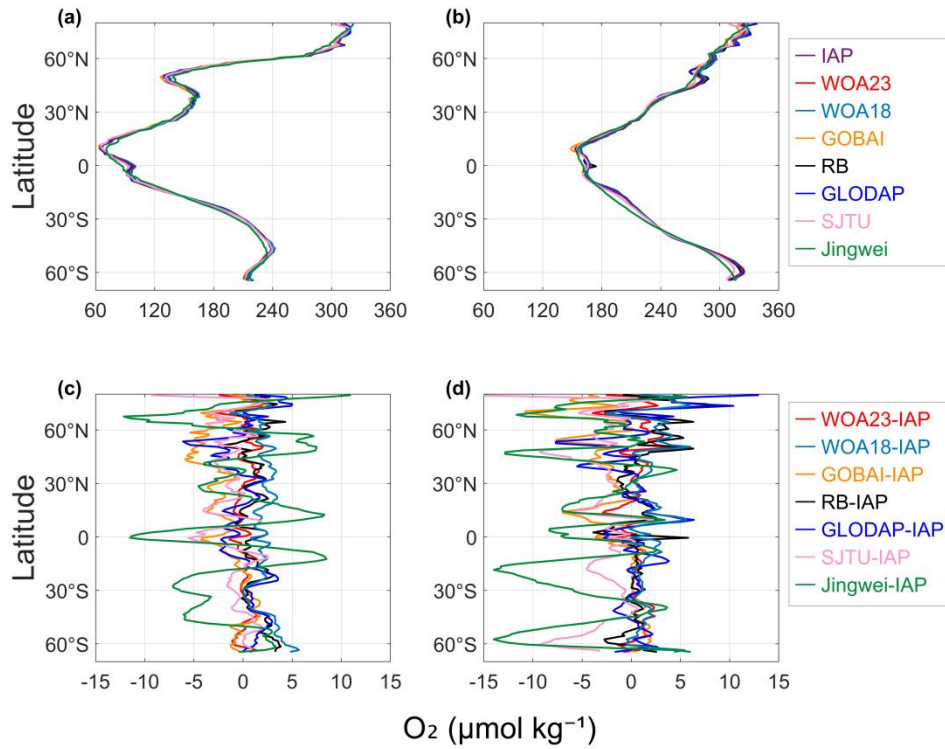
248 The global zonal mean O_2 concentration of the eight datasets for the upper 1000 m
 249 shows consistency for the zonal structure (Fig. 4a). There is a minimum of mean O_2 levels
 250 around the tropical regions for all the datasets, associated with a shoaling of the tropical and
 251 subtropical thermocline depth (Deutsch et al., 2011) and the presence of the tropical upper
 252 ocean OMZ. The differences in the global zonal mean O_2 for the upper 1000 m between the
 253 seven data products (WOA23, WOA18, GOBAI, RB, GLODAP, SJTU, and Jingwei) and
 254 IAP are shown in Fig. 4b. The differences in zonal mean 0-1000 m averaged O_2 are mostly
 255 within $\sim 5 \mu\text{mol kg}^{-1}$. The zonal mean O_2 difference between IAP and WOA23 is the smallest,
 256 which is generally within $\sim 1.5 \mu\text{mol kg}^{-1}$. The zonal mean of GOBAI is generally lower than
 257 that of IAP, especially in the Northern Hemisphere, which may imply stronger deoxygenation

258 trends in the Northern Hemisphere, as the GOBAI climatology baseline is newer than that of
259 IAP. The zonal mean of the RB dataset is higher than that of IAP by $\sim 0.78 \mu\text{mol kg}^{-1}$ on
260 average, consistent with the positive offset shown in Fig. 3. Jingwei dataset has the strongest
261 differences from IAP and other products, showing a notable zonal fluctuation.

262 The results for the depth layers 0-600 m and 0-2000 m (Fig. S2) show similar variation
263 pattern to the depth layer 0-1000 m. The differences in the global zonal mean O_2 between
264 data products are mostly within $\sim 5 \mu\text{mol kg}^{-1}$ for 0-600 m and within $\sim 3 \mu\text{mol kg}^{-1}$ for 0-2000
265 m (Fig. S2b, S2d). For 0-600 m, the zonal mean O_2 difference between IAP and WOA23 is
266 the smallest and Jingwei shows the strongest differences from IAP and other products. For 0-
267 2000 m, the depth average makes the difference between datasets much smaller. Jingwei still
268 shows relatively large discrepancy from the other datasets in the regions around 60°N and
269 the equator. Within the latitude range 20°S - 50°S where all other data products show the best
270 agreement, Jingwei exhibits a significant deviation of $\sim 5 \mu\text{mol kg}^{-1}$ from the rest.

271 However, the zonal mean O_2 concentration for 0-100 m (Fig. 4b) shows a relatively
272 distinct pattern. The zonal mean O_2 decreases linearly with the decrease of latitude for all the
273 datasets, except that for the high latitude range 60°S - 80°S , the zonal mean O_2 profiles
274 maintain a relatively stable value and the estimations between different data products vary to
275 an extent of $\sim 20 \mu\text{mol kg}^{-1}$ (Fig. 4d), which illustrates the relatively higher uncertainty in the
276 data reconstruction in this high latitude range.

277



278

279 **Figure 4** Global zonal mean O₂ concentration and differences for 0-1000 m (a, c) and 0-100
 280 m (b, d) (unit: μmol kg⁻¹).

281

282 3.3 Spatial pattern

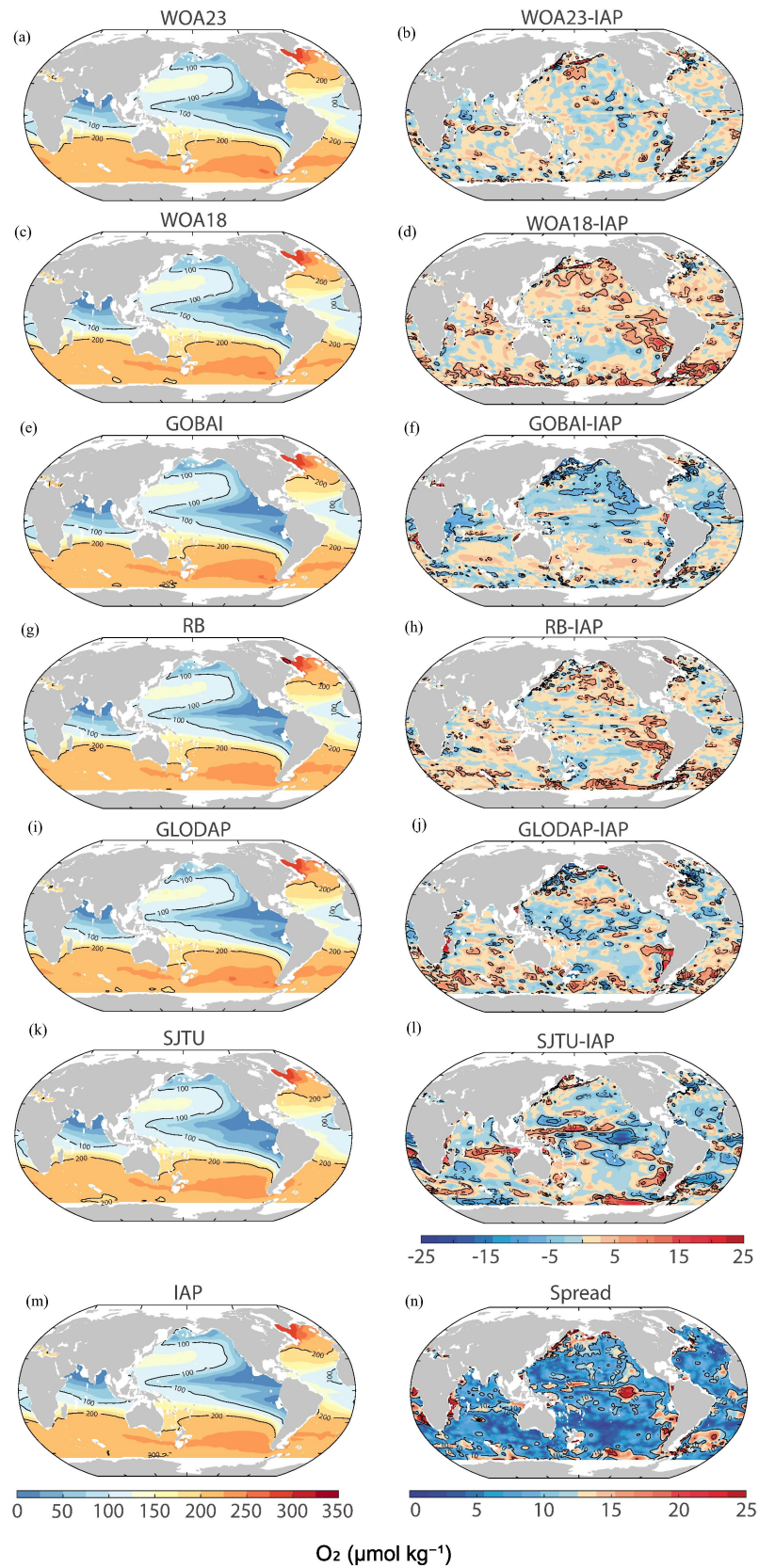
283 The spatial distribution of the upper 1000 m mean O₂ and the difference between IAP
 284 and six other datasets is shown in Fig. 5a-m. The dataset of Jingwei is not included because
 285 the spatial maps are not currently available. The difference of the 0-1000 m mean O₂ is
 286 mainly within the magnitude of ~15 μmol kg⁻¹, which shows substantial local differences
 287 even though their differences are relatively small when averaged globally (~3 μmol kg⁻¹, Fig.
 288 3). The mean O₂ of the GOBAI dataset is generally lower than IAP for 0-1000m (Fig. 5f),
 289 consistent with the conclusions from the previous comparisons. There are bigger differences
 290 located in the regions such as the subpolar North Pacific, the Southern Ocean fronts, and the
 291 eastern Pacific regions close to OMZ boundaries, where the strong spatial O₂ gradient, makes
 292 the reconstruction sensitive to the mapping process and data distribution (Ito et al., 2025).
 293 GOBAI, SJTU, and GLODAP show a negative difference (~-15 μmol kg⁻¹) compared to IAP
 294 for the upper 1000 m mean O₂ in most of the north and equatorial Pacific Ocean, and
 295 equatorial Atlantic Ocean. WOA23 and GOBAI show a similar pattern of difference in the
 296 Indian and Pacific Oceans: more positive offsets in the eastern Pacific/Indian Oceans and
 297 negative offsets in the western Pacific/Indian Oceans. For the two generations of WOA

298 products, the difference between WOA23 and IAP is more negative globally than the
299 difference between WOA18 and IAP, likely due to the use of more recent data in WOA23.
300 SJTU exhibits a distinct pattern of differences, with substantial negative differences
301 occurring in the tropics.

302 The spatial map of the spread of the upper 1000 m mean climatological O₂ among all the
303 datasets except Jingwei is presented in Fig. 5n. The spread here is defined as the maximum
304 absolute value of the differences between all the other products and IAP. The spread is within
305 12 μmol kg⁻¹ in most of the ocean areas, with the largest spread reaching 25 μmol kg⁻¹ where
306 strong spatial O₂ gradients exist. The spread is generally lower in the Southern Hemisphere
307 than in the Northern Hemisphere, in contrast to the fact that there are more observations in
308 the North. This might be related to three issues: 1) A common error in the mapping method,
309 where the spatial interpolation generates over-smoothed or similar-biased fields in the
310 Southern Hemisphere; 2) the variability is lower in the Southern Hemisphere than in the
311 Northern Hemisphere, which reduces the reconstruction errors in the Southern Hemisphere; 3)
312 the deoxygenation trends are higher in the Northern Hemisphere than in the Southern thus the
313 spread reveals the O₂ level at different periods.

314 The exact reason can be explored with single-factor reconstruction experiments such as
315 those performed by Ito et al. (2025), which use the same input data but different mapping
316 methods to isolate the impact of mapping on climatology reconstruction. Further analyses are
317 required, but it is useful to know the differences between the products. When comparing the
318 depth-mean O₂ between the eight datasets we adopted here which didn't distinguish different
319 impact factors in the process of generating gridded data products and aimed to illustrate a
320 comprehensive discrepancy, the difference for all the datasets for 0-300 m is within ±25
321 μmol kg⁻¹ and the spread is up to 35 μmol kg⁻¹ (Fig. S3). The regions of high variability
322 mainly locate in the tropical and East Pacific, subpolar North Pacific and Southern Ocean
323 fronts where there are strong spatial O₂ gradients. However, when using the same quality-
324 controlled observational data as input and constraining the impact on data reconstruction to
325 only the mapping method, the difference of the mapped O₂ concentration between different
326 mapping methods is within ±10 μmol kg⁻¹ for 0-300 m (Ito et al., 2025). The overall
327 difference between the data products is more than two times of the difference constrained to a
328 single factor of the mapping method, indicating that the other factors, such as the quality
329 control technique, bias correction, vertical interpolation, and so on, also contribute to the
330 uncertainty source to a large extent. Further analyses are required to assess and quantify the

331 impact of every individual procedure on the whole process of O₂ data reconstruction, but it is
 332 useful to know the differences between the data products as a start.
 333



334

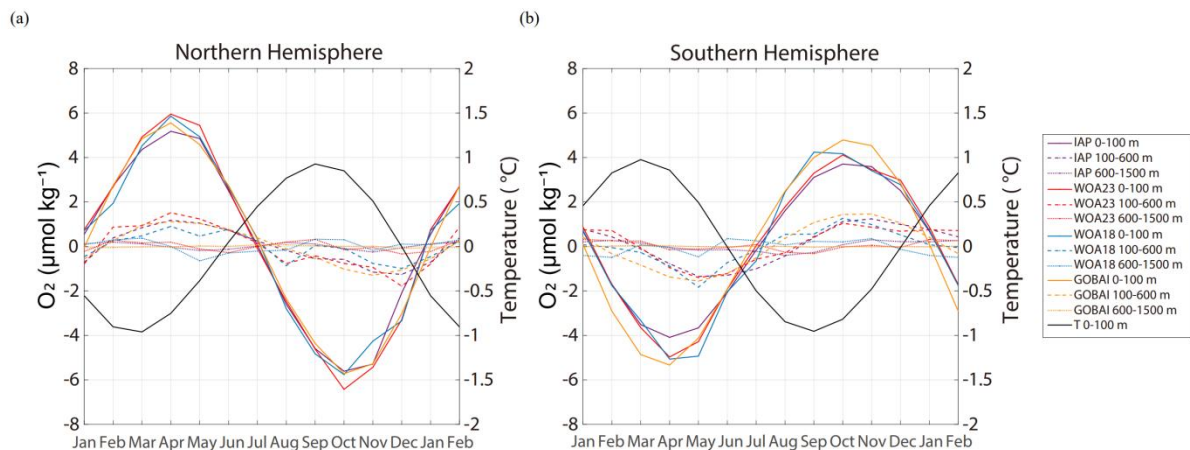
335 **Figure 5** The spatial patterns of the upper 1000 m climatological mean O₂ concentration
 336 (unit: $\mu\text{mol kg}^{-1}$). (a) WOA23, (b) WOA23-IAP, (c) WOA18, (d) WOA18-IAP, (e) GOBAI,
 337 (f) GOBAI-IAP, (g) RB, (h) RB-IAP, (i) GLODAP, (j) GLODAP-IAP, (k) SJTU, (l) SJTU-
 338 IAP, (m) IAP, (n) Spread is calculated as the difference of the upper 1000 m climatological
 339 mean O₂ among the datasets.

340

341 3.4 Annual cycle

342 The annual cycle of the four products that provide a monthly climatology (IAP,
 343 WOA23, WOA18, and GOBAI) is presented in Fig. 6 for the 0-100 m, 100-600 m, and 600-
 344 1500 m, and for Northern and Southern hemispheres, respectively calculated by the monthly
 345 anomalies derived by subtracting the annual mean climatology of every data product
 346 respectively. The annual cycle of the 0-100 m temperature for northern and southern
 347 hemispheres is also calculated using the gridded temperature climatology product of IAP
 348 (Cheng et al., 2024). The magnitude of the O₂ seasonal cycle, defined as the maximum
 349 amplitude of the annual variation, is greatest near the surface and decreases with depth.
 350 Specifically, it is approximately $6 \mu\text{mol kg}^{-1}$ for the 0-100 m layer and $2 \mu\text{mol kg}^{-1}$ for the
 351 deeper layer (100-600 m). The reduced annual cycle with depth is associated with stronger
 352 annual variations of ocean temperature, wind-driven ventilation, and biological processes in
 353 the upper ocean compared to the deep ocean.

354



355

356 **Figure 6** Annual variation of the (a) Northern Hemisphere and (b) Southern Hemisphere
 357 global mean O₂ for IAP, WOA23, WOA18, and GOBAI datasets.

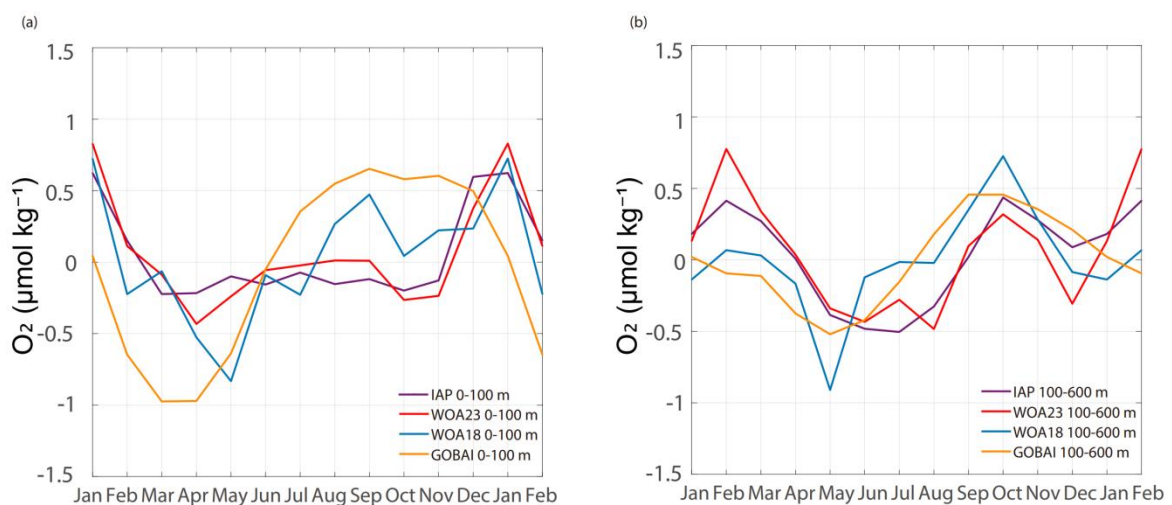
358

359 The appearance time of maximum (Apr.) and minimum (Oct.) O₂ levels in the northern
 360 hemisphere are consistent among the four datasets for 0-100 m global mean O₂. Moreover,

361 the O₂ maximum in the depth layer in the northern and southern hemispheres for 0-100 m
 362 lags about one month behind the temperature change, reflecting that besides the dominant
 363 thermal induced increase in O₂ solubility, some physical/biological processes also impact the
 364 concentration of ocean O₂ (Garcia et al., 2005; Wang et al., 2022). For the northern
 365 hemisphere, the annual variation of the subsurface 100-600 m layer also shows a pattern of
 366 annual cycle with the maximum (Apr.) and minimum (Dec.) similar to the surface 0-100 m
 367 layer, indicating that the O₂ annual cycle could penetrate to the deeper layer of ~600 m. It is
 368 primarily due to the mechanisms including climatological winter mixed layer deepening,
 369 which ventilates the subsurface, and seasonal thermocline dynamics coupled with organic
 370 matter remineralization (Stamma et al., 2010). For the southern hemisphere, similar patterns
 371 also exist.

372 Although the two hemispheric O₂ annual cycles can be well-defined, the global mean is
 373 more subtle, as different products show large differences in patterns of the global mean
 374 annual cycle (Fig. 7). It appears that global 100-600 m O₂ annual cycles are more consistent
 375 across data products than 0-100 m, probably associated with noisier data and more natural
 376 variability near the sea surface. For global 100-600 m O₂, all datasets suggest an O₂ reduction
 377 from March to September and an increase from October to February, consistent with the
 378 Southern Hemisphere changes (Fig. 7b versus Fig. 6b). The magnitude of the global 0-100 m
 379 and 100-600 m annual cycle ranges from -1 μmol kg⁻¹ to 0.8 μmol kg⁻¹ for the four datasets,
 380 but the standard deviations among the four datasets are ~0.3 μmol kg⁻¹ (0-100 m) and ~0.2
 381 μmol kg⁻¹ (100-600 m), indicating a similar level of signal and noise (Fig. 7).

382



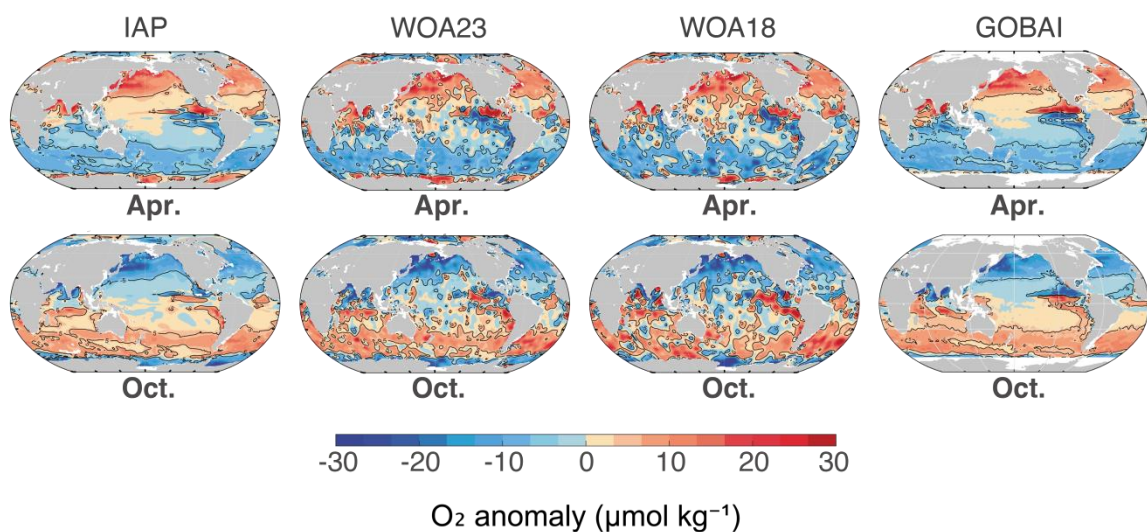
383

384 **Figure 7** Global annual variation of the (a) 0-100 m and (b) 100-600 m global mean O₂ for
 385 IAP, WOA23, WOA18, and GOBAI datasets.

386

387 The annual cycle of O₂ anomalies shows a distinct spatial pattern (0-100 m mean O₂,
388 Apr. versus Oct., Fig. 8). The anomalies are calculated by subtracting the annual mean from
389 the monthly climatologies for the four datasets (IAP, WOA23, WOA18, and GOBAI)
390 respectively. In April, the O₂ anomalies of 0-100 m in most of the northern hemisphere are
391 positive, and they turn negative in October. The tropical ocean annual cycle is not easily
392 defined, as many regions have semi-annual variability. Different products exhibit a consistent
393 pattern of change, whereas the detailed structures are quite distinct. In general, WOA23 and
394 WOA18 have more patchy characteristics than IAP and GOBAI, likely related to the
395 mapping methods employed by each: WOA uses an anti-distance weighted function to
396 interpolate the field; on the other hand, IAP uses model simulations to provide covariance
397 and GOBAI takes advantage of correlations between O₂ and temperature and salinity, both
398 building physical ocean properties into the reconstruction.

399



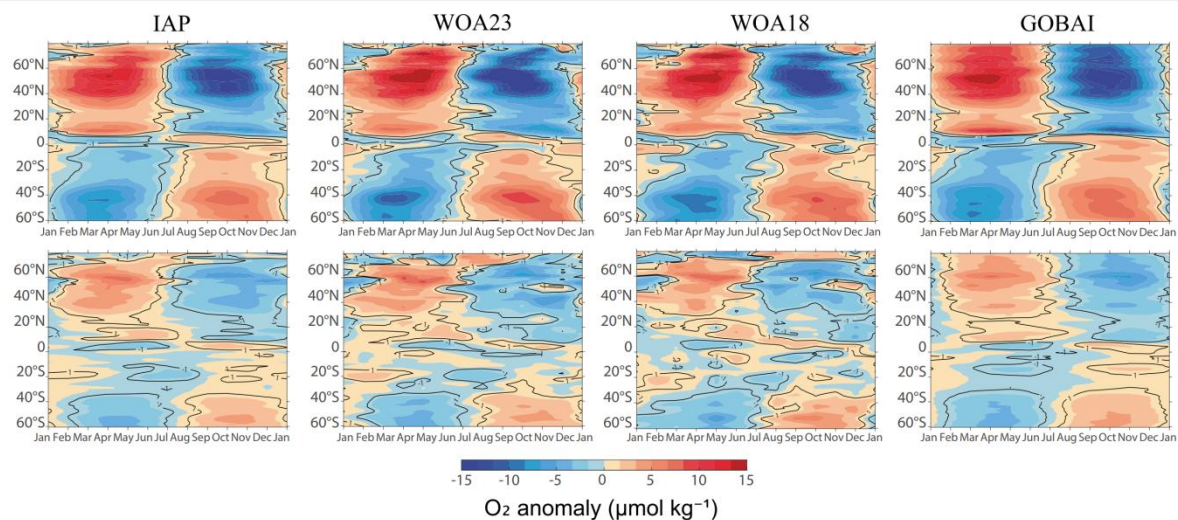
400

401 **Figure 8** Spatial distribution of the O₂ anomaly (0-100 m) for the IAP, WOA23, WOA18,
402 and GOBAI climatology.

403

404 The zonal mean structure of the annual cycle is shown in Fig. 9, and all the datasets
405 show similar annual cycle patterns with some difference in smoothness and magnitude for
406 both 0-100 m and 100-600 m mean O₂. For 0-100 m, the largest seasonal changes occur in
407 the extra-tropics in the 30° N to 60° N belts of the Northern hemisphere. In the Southern
408 hemisphere, the largest seasonal changes occur in the latitudinal band centered near 40° S.
409 For both 0-100 m and 100-600 m, the phase transitions occur around Jul. and Jan. for all

410 datasets, which are consistent with the annual variation analysis in Fig. 6. The phase change
 411 of O_2 lags about one month behind the temperature change (Jun. and Dec. as shown in Fig.
 412 S4), reflecting that some physical/biological processes also impact the concentration of O_2
 413 besides the dominant thermally induced increase in O_2 solubility. Semi-annual cycles near the
 414 equator are visible in the upper ocean for almost all products. There is a distinction of the
 415 annual cycle at about 10° N, corresponding to the location of the intertropical convergence
 416 zone (ITCZ) (Garcia et al., 2005).



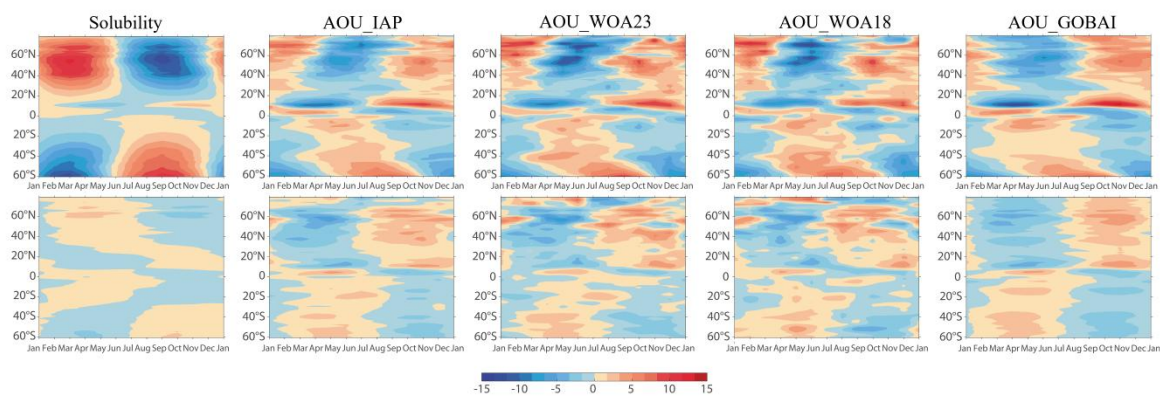
417
 418 **Figure 9** Zonal mean annual cycles for 0-100 m (upper) and 100-600 m (lower) for different
 419 data products (IAP, WOA23, WOA18, and GOBAI).

421 The zonal mean annual cycles of solubility and Apparent Oxygen Utilization (AOU) of
 422 different data products for 0-100 m and 100-600 m are shown in Fig. 10. The solubility is
 423 calculated using the gridded temperature and salinity products of IAP (Cheng et al., 2024)
 424 following the Garcia and Gordon (1992) method. Generally, the zonal 0-100 m O_2 seasonal
 425 cycle is mainly dominated by the solubility, whereas the AOU dominates the 100-600 m O_2
 426 pattern.

427 For 0-100 m, the AOU seasonal cycle in the mid-latitude is about two to three months
 428 lagging that of the temperature/solubility seasonal variation (Figs. 6, 10, S4). Within 20° N-
 429 60° N, the zonal mean AOU anomaly of 0-100 m is mostly negative from March to August.
 430 The phase transition of AOU occurs in March, which corresponds to the temperature
 431 minimum/solubility maximum. And AOU reaches a minimum in about May/June,
 432 corresponding to the phase transition of the zonal mean temperature/solubility anomaly (Fig.
 433 S4, 10). A possible explanation is from the combined impacts of biological and physical
 434 processes. The spring phytoplankton bloom lags the onset of temperature increase (starting in

435 Mar.) because phytoplankton proliferation requires sufficient light from increasing spring
 436 insolation and nutrient entrainment due to a shallower mixed layer (Martin, 2012). And the
 437 net community production (NCP, the difference between gross community photosynthesis
 438 and community respiration) reaches a maximum in about May (Wang et al., 2022). The
 439 solubility reaches a minimum in September, which corresponds with the phase change of
 440 AOU. And the maximum of AOU lags about two months behind the temperature
 441 maximum/solubility minimum, which is also a combined effect of the prolonged response
 442 time of biological processes and the physical processes possibly induced by the deepening
 443 autumn mixed layer. The situation in 20° S-60° S is similar to 20° N-60° N for 0-100 m,
 444 mainly with the signs reversed. For 100-600 m, the annual variation in temperature/solubility
 445 is relatively small, and the pattern of AOU variation dominates, with the underlying
 446 processes requiring further investigation.

447



448

449 **Figure 10** Zonal mean annual cycles of the solubility and AOU anomaly of different data
 450 products (AOU_IAP, AOU_WOA23, AOU_WOA18, and AOU_GOBAL) for 0-100 m
 451 (upper) and 100-600 m (lower) (unit: $\mu\text{mol kg}^{-1}$).

452

453 To assess the patterns of annual cycle regionally, the zonal mean structures of the annual
 454 cycle for different ocean basins are shown in Figs. S5-S7. Distinct seasonal changes exist in
 455 the Pacific, Atlantic and Indian Oceans. The annual cycle patterns for the Pacific and Atlantic
 456 Ocean coincide with the global O_2 annual cycle both for the 0-100 m and 100-600 m layers
 457 closely. For the Indian Ocean, there are larger seasonal changes in the latitude range of $\sim 10^\circ$ -
 458 20° N for 0-100 m than the Pacific and Atlantic Oceans. The annual variations of the mean
 459 O_2 for three major ocean basins (Pacific, Atlantic, Indian) for 0-100 m and 100-600 m are
 460 shown in Figs. S8-S10, and also for the North and South Pacific/Atlantic, respectively, in
 461 Figs. S11-S12. The magnitude of the O_2 seasonal cycle is greatest in the Atlantic Ocean (~ 3

462 $\mu\text{mol kg}^{-1}$) for the 0-100 m layer, which corresponds to a magnitude of $\sim 6 \mu\text{mol kg}^{-1}$ in the
463 North Atlantic and $\sim 4 \mu\text{mol kg}^{-1}$ in the South Atlantic. The minimum and maximum O_2 levels
464 ($-4 \mu\text{mol kg}^{-1}$ to $6 \mu\text{mol kg}^{-1}$) and also occurrence time (Jul./Oct.) of WOA18 for 0-100 m
465 differ the most from those of the other three datasets in the South Atlantic (Fig. S12b).

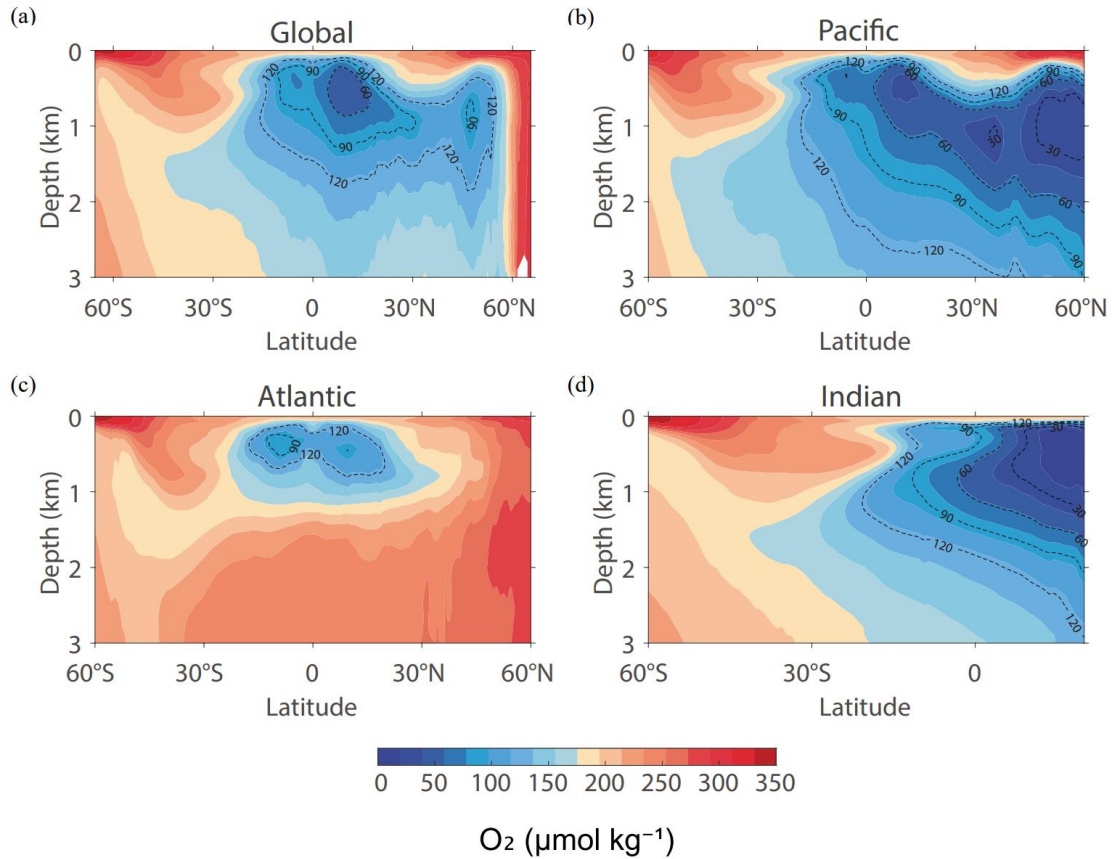
466

467 **3.5 Oxygen minimum zones**

468 Oxygen minimum zones (OMZ) are important regions that impact marine organism
469 distributions and biogeochemical cycling. OMZ occur in various regions such as the tropical
470 Pacific and Atlantic Oceans, the North Pacific Ocean, and the North Indian Ocean, posing
471 challenges for marine organisms adapted to higher O_2 concentrations (Strammer et al., 2021).
472 In various studies, OMZ are bounded by different thresholds of O_2 levels. Here, we select
473 two typical thresholds of $60 \mu\text{mol kg}^{-1}$ and $90 \mu\text{mol kg}^{-1}$ to define OMZ (Ito et al., 2025),
474 referred to as OMZ60 and OMZ90, respectively.

475 The zonal mean O_2 of the IAP climatology dataset for global and three major basins are
476 shown in Fig. 11. Globally, the zonal mean OMZ90 regions are mainly located within 200-
477 1200 m and 5°S - 30°N , associated with upwelling and high O_2 consumption. The Pacific
478 Ocean contains the largest volume of OMZ60 and OMZ90 among the three ocean basins,
479 with the OMZ90 extending from $\sim 15^\circ \text{S}$ to $\sim 60^\circ \text{N}$ and from a depth of ~ 200 m to ~ 3000 m.
480 There is a gradual increase in the max depth of OMZ90 and OMZ60 in the Pacific Ocean
481 from $\sim 15^\circ \text{S}$ to $\sim 60^\circ \text{N}$; thus, the OMZ in the North Pacific Ocean has greater vertical extent.
482 The OMZ in the North Pacific Ocean is also more severe because there is a notable region
483 with zonal O_2 levels less than $30 \mu\text{mol kg}^{-1}$ in the ~ 700 to ~ 1500 m layer. The OMZ90 in the
484 Indian Ocean extends from $\sim 10^\circ \text{S}$ to the northernmost end and is located from ~ 20 down to a
485 maximum depth of 1800 m. In the Atlantic Ocean, the OMZ90 is located within a 300-500 m
486 layer, with an area much smaller than that of the Pacific and Indian Oceans (Table 2).

487



488

489 **Figure 11** Comparison of zonal mean O₂ climatology (IAP climatology, unit: $\mu\text{mol kg}^{-1}$) in
 490 the (a) Global Ocean, (b) Pacific, (c) Atlantic, and (d) Indian Oceans.

491

492 We also calculated the volume of OMZ60 and OMZ90 globally and for each basin in
 493 Table 2 using six datasets (excluding GOBAI and SJTU because their maximum depth only
 494 reaches about 2000 m below the ocean surface). The global volume of OMZ60 and OMZ90
 495 is generally consistent among the datasets, with a standard deviation of 1.95 % and 1.72 %
 496 across the products for OMZ60 and OMZ90, respectively. The Pacific Ocean contains most
 497 of the OMZ (83.05 % of the global OMZ60 and 81.29 % of the global OMZ90), with a
 498 standard deviation of 3.93 % and 2.37 % across the products. The Atlantic Ocean contains
 499 about 1.04 % and 2.38 % of the global OMZ60 and OMZ90, respectively, which is the lowest
 500 among the three ocean basins. The standard deviation is 20.24 % and 10.77 % for the Atlantic
 501 Ocean OMZ60 and OMZ90, respectively. The estimated OMZ for the Atlantic Ocean may be
 502 more sensitive to the horizontal resolution, mapping method, and so on.

503

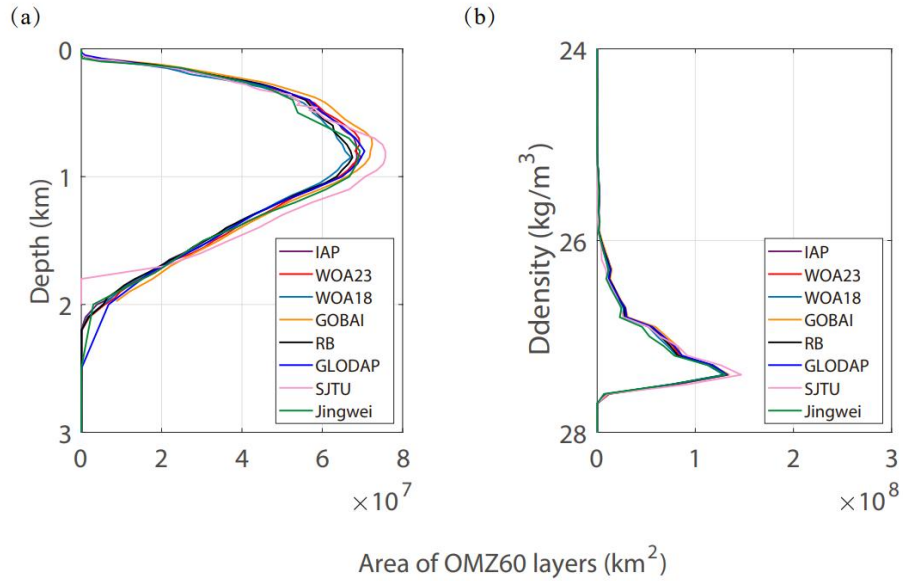
504 **Table 2** The volume of OMZ60 and OMZ90 calculated from the annual mean climatology
 505 for each basin and for different products. The values are in the units of 10^6 km^3 .

	OMZ60				OMZ90			
Datasets	Global	Pacific	Atlantic	Indian	Global	Pacific	Atlantic	Indian
IAP	81.76	68.98	0.85	11.91	152.78	125.56	3.83	23.36
WOA23	83.79	69.90	0.88	12.49	155.46	126.86	3.72	24.33
WOA18	79.42	66.71	0.74	11.46	152.23	124.93	3.50	23.28
RB	80.93	67.73	0.94	11.74	152.69	124.95	3.93	23.26
GLODAP	80.68	68.18	1.07	11.42	146.69	119.85	3.93	22.90
Jingwei	78.99	61.74	0.52	12.63	152.14	119.19	2.81	23.70
Mean	80.92	67.21	0.84	11.94	152.00	123.56	3.62	23.47
Standard Deviation	1.58	2.64	0.17	0.47	2.62	2.93	0.39	0.45

506

507 The OMZ areas as a function of depth and density are shown in Fig. 12. The density
508 layers are calculated with the Gibbs-SeaWater Oceanographic Toolbox (IOC et al., 2010;
509 McDougall & Barker, 2011; Kwiecinski and Babbin, 2021), using the gridded temperature
510 and salinity climatology products of IAP (Cheng et al., 2024). The maximum OMZ60 area
511 occurs at a depth of ~800 m and a density of 27.75 kg m⁻³ for all the datasets. Most OMZ60s
512 exist in the upper 2000 m. So that all the climatologies including GOBAI and SJTU with the
513 maximum depth of 2000 m could be involved in the analysis of OMZ areas at depth levels.
514 GOBAI and SJTU exhibit a larger OMZ60 volume within the upper 2000 m compared to
515 other products, and the maximum depth of SJTU OMZ60 is ~1700 m, which is shallower
516 than that of the other products. At density levels, the products are very consistent, and SJTU
517 shows a larger area of OMZ60 near the 27.4 kg m⁻³ level and Jingwei shows a smaller area of
518 OMZ60 near the 27 kg m⁻³ level.

519

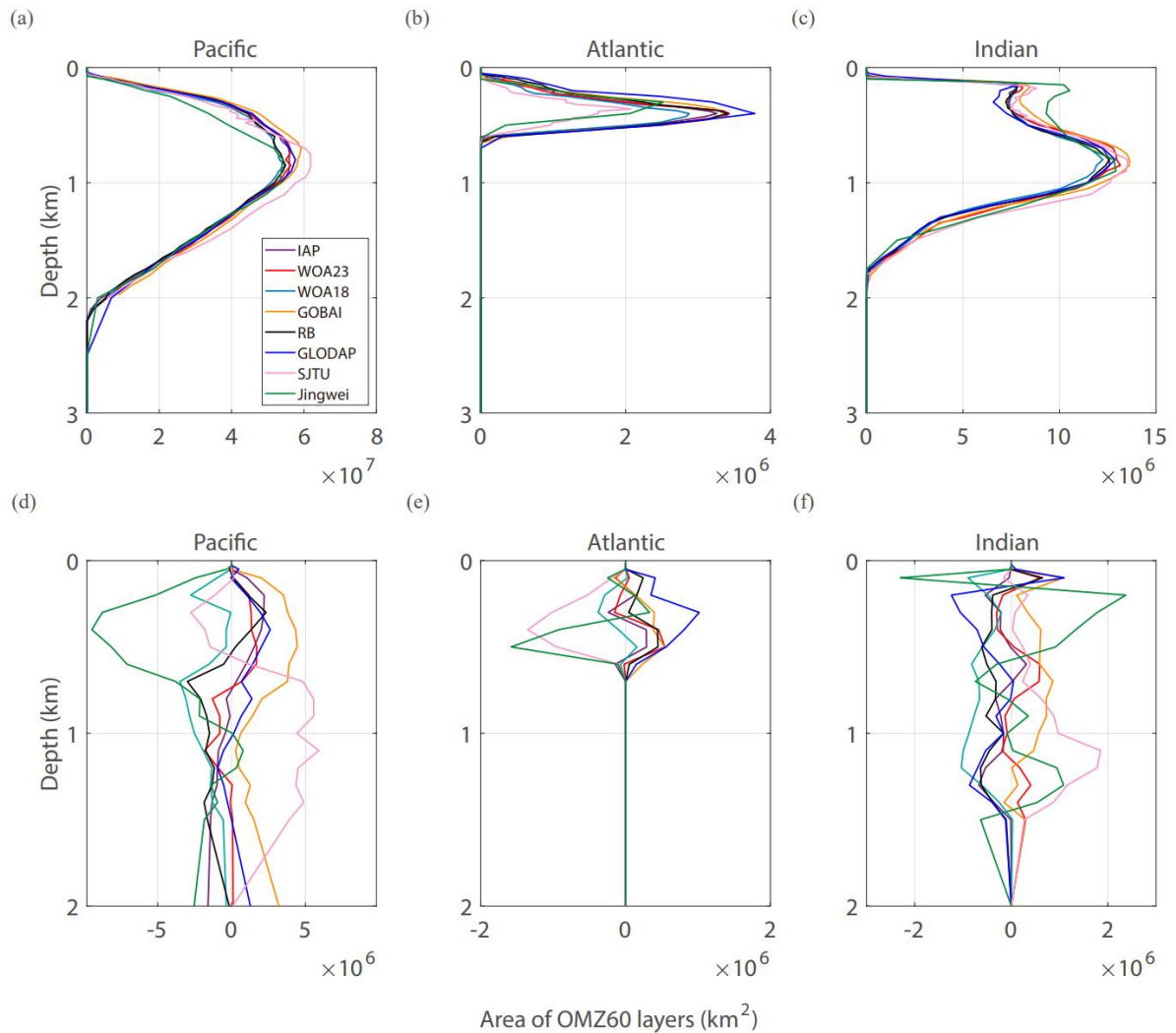


520

521 **Figure 12** The global horizontal area of OMZ60 in each interpolated layer with respect to
 522 (a) depth and (b) density.

523

524 Figure 11a-c shows the horizontal OMZ60 area at depth levels for the Pacific, Atlantic,
 525 and Indian Oceans, respectively. Consistent with the volume assessment in Table 2, the
 526 Pacific Ocean contains the largest OMZ60 area, followed by the Indian and Atlantic Oceans.
 527 The maximum OMZ60 area occurs at a depth of about 800 m in the Pacific and Indian
 528 Oceans, but at a much shallower depth of ~400 m in the Atlantic Ocean. Jingwei shows the
 529 largest difference from the other products in the Pacific and Indian Oceans at the upper 500
 530 m depth. SJTU shows a larger area of OMZ60 in the Pacific and Indian Oceans but a smaller
 531 area in the Atlantic Ocean than the other products (Fig. 13). Collectively, different products
 532 show a spread of $\pm 4 \times 10^6 \text{ km}^2$ for the Pacific OMZ60 and of $\pm 1 \times 10^6 \text{ km}^2$ for the Indian and
 533 Atlantic OMZ60 (Fig. 13d-f), except that Jingwei shows a very large difference of up to -9
 534 $\times 10^6 \text{ km}^2$ at the depth around 500 m for the Pacific OMZ60 area compared to the ensemble
 535 mean (Fig. 13d).



536

537 **Figure 13** OMZ60 area for the Pacific, Atlantic, and Indian Oceans in units of 10^6 km^2 . The
 538 upper row is the vertical distribution of the OMZ areas: (a) Pacific, (b) Atlantic, (c) Indian.
 539 The lower row is the differences in the OMZ areas relative to the ensemble mean: (d) Pacific,
 540 (e) Atlantic, (f) Indian.

541

542 **4 Conclusion**

543 Observationally-based gridded data products provide a basis for detecting and
 544 understanding ocean O_2 changes at various spatial and temporal scales. These observational
 545 datasets are also used to validate the computational ocean biogeochemistry and earth system
 546 models. This study provides a quantitative description of the O_2 climatology, annual cycle,
 547 and OMZ distribution with eight O_2 data products. There have been several new O_2 data
 548 products developed in recent years, which makes this comparative analysis timely.

549 The global mean O_2 shows a well-established high-low-high vertical structure and a
 550 good consistency among all products. The global mean O_2 concentrations of the products

551 over depth generally agree within $\pm 3 \mu\text{mol kg}^{-1}$. Regionally, the gridded mean difference of
552 the 0-1000 m mean O_2 is mainly within $\sim 12 \mu\text{mol kg}^{-1}$. For the global 0-100 m O_2 annual
553 cycle, O_2 anomalies (differences from the annual mean) ranges from $-1 \mu\text{mol kg}^{-1}$ to $0.8 \mu\text{mol}$
554 kg^{-1} , but the inter-products difference (defined by the standard deviation of four datasets that
555 provide a monthly climatology) can be as large as $\sim 0.3 \mu\text{mol kg}^{-1}$, indicating a similar signal-
556 to-noise ratio among the four datasets of monthly climatology. We also analyzed the OMZ
557 distribution for different climatology datasets. Different products show a spread of $\pm 4 \times 10^6$
558 km^2 for the Pacific OMZ60 and $\pm 1 \times 10^6 \text{ km}^2$ for the Indian and Atlantic OMZ60.

559 The assessments presented in this study demonstrate the consistency and differences
560 among available products, supporting their future use. Substantial local differences ($\pm 25 \mu$
561 mol kg^{-1} for the upper 1000 m climatological mean) can be seen, which could influence the
562 baseline from which anomalies and trends are calculated and could give an insight into
563 regions that are relatively more sensitive in the process of gridded data reconstruction, such
564 as the subpolar North Pacific, the Southern Ocean fronts, and the eastern Pacific regions
565 close to OMZ boundaries where the spatial O_2 gradient is large.

566 The overall spread across products results from all uncertainty sources (e.g.,
567 measurement errors, mapping errors, different time periods, etc.). Controlled
568 intercomparisons that isolate each uncertainty source are needed in the future to understand
569 the contribution of a single factor, especially in regions showing a large spread. It will
570 eventually help the community to improve the methodologies and reduce the spread in the
571 future. Another caveat is that only a limited number of products are included in this inter-
572 comparison. We hope to maintain and extend this activity in the future and serve as a regular
573 intercomparison exercise to provide critical information to the data users.

574

575 **Data availability**

576 All the gridded data products used in this study are available at:

577 GODIP-DO Group: Global Dissolved Oxygen Gridded Climatological Datasets, Zenodo[data
578 set], <https://doi.org/10.5281/zenodo.16664650>. 2025.

579

580 **Author contributions**

581 JD and LC-conceptualization, supervision, methodology; JD-formal analysis, visualization,
582 writing; JD, LC, HEG, ZW, JDS, CJR, YZ and BL-data curation; TI, HEG, ZW, JDS, GGN,
583 SMB and SM-writing.

584

585 **Competing interests**

586 The contact author has declared that none of the authors has any competing interests.

587

588 **Financial support**

589 IAP authors gratefully acknowledge support by National Natural Science Foundation of
590 China (grant no. 42261134536), the new Cornerstone Science Foundation through the
591 XPLOER PRIZE and the Asian Cooperation Fund, and the International Partnership
592 Program of the Chinese Academy of Sciences (Grant No. 060GJHZ2024064MI). TI and JDS
593 are supported by funding from the US National Science Foundation (OCE-2446011,
594 2446012). This is CICOES contribution no. 2025-1474 and PMEL contribution no. 5797.

595

596 **References**

597 Bindoff, N. L., Cheung, W. W. L., Kairo, J. G., Aristegui, J., Guinder, V. A., Hallberg, R.,
598 Hilmi, N., Jiao, N., Karim, M. S., Levin, L., O'Donoghue, S., Purca Cuicapusa, S. R.,
599 Rinkevich, B., Suga, T., Tagliabue, A., and Williamson, P.: Changing Ocean, marine
600 ecosystems, and dependent communities, In: IPCC Special Report on the Ocean and
601 Cryosphere in a Changing Climate, Cambridge University Press, Cambridge, UK and
602 New York, NY, USA, 447-587, <https://doi.org/10.1017/9781009157964.007>, 2019.

603

604 Boyer, T. P., Baranova, O. K., Coleman, C., Garcia, H. E., Grodsky, A., Locarnini, R. A.,
605 Mishonov, A. V., Paver, C. R., Reagan, J. R., Seidov, D., Smolyar, I. V., Weathers, K.,
606 and Zweng, M. M.: World Ocean Database 2018, Mishonov, A. V., Technical Editor,
607 NOAA Atlas NESDIS 87, 2018.

608

609 Breitburg, D., Levin, L. A., Oschlies, A., Grégoire, M., Chavez, F. P., Conley, D. J., Garçon,
610 V., Gilbert, D., Gutiérrez, D., Isensee, K., Jacinto, G. S., Limburg, K. E., Montes, I.,
611 Naqvi, S. W. A., Pitcher, G. C., Rabalais, N. N., Roman, M. R., Rose, K. A., Seibel, B.
612 A., Telszewski, M., Yasuhara, M., and Zhang, J.: Declining oxygen in the global ocean
613 and coastal waters, *Science*, 359, eaam7240, <https://doi.org/10.1126/science.aam7240>,
614 2018.

615

616 Cheng, L. and Zhu, J.: Benefits of CMIP5 Multimodel Ensemble in Reconstructing Historical
617 Ocean Subsurface Temperature Variations, *J. Clim.*, 29, 5393-5416,
618 <https://doi.org/10.1175/JCLI-D-15-0730.1>, 2016.

619

620 Cheng, L., Trenberth, K. E., Fasullo, J., Boyer, T., Abraham, J., and Zhu, J.: Improved
621 estimates of ocean heat content from 1960 to 2015, *Sci. Adv.*, 3, e1601545,
622 <https://doi.org/10.1126/sciadv.1601545>, 2017.

623

624 Cheng, L., Pan, Y., Tan, Z., Zheng, H., Zhu, Y., Wei, W., Du, J., Yuan, H., Li, G., Ye, H.,
625 Gouretski, V., Li, Y., Trenberth, K. E., Abraham, J., Jin, Y., Reseghetti, F., Lin, X.,
626 Zhang, B., Chen, G., Mann, M. E., and Zhu, J.: IAPv4 ocean temperature and ocean heat

627 content gridded dataset, *Earth Syst. Sci. Data*, 16, 3517-3546,
628 <https://doi.org/10.5194/essd-16-3517-2024>, 2024.
629

630 Deutsch, C., Brix, H., Ito, T., Frenzel, H., and Thompson, L.: Climate-forced variability of
631 ocean hypoxia, *Science*, 333, 336-339, <https://doi.org/10.1126/science.1202422>, 2011.
632

633 Garcia, H.E. and Gordon, L.I.: Oxygen solubility in seawater: Better fitting equations,
634 *Limnol. Oceanogr.*, 37, 1307-1312, <https://doi.org/10.4319/lo.1992.37.6.1307>, 1992.
635

636 Garcia, H. E., Boyer, T. P., Levitus, S., Locarnini, R. A., and Antonov, J.: On the variability
637 of dissolved oxygen and apparent oxygen utilization content for the upper world ocean:
638 1955 to 1998, *Geophys. Res. Lett.*, 32, L09604, <https://doi.org/10.1029/2004GL022286>,
639 2005.
640

641 Garcia, H. E., Boyer, T. P., Levitus, S., Locarnini, R. A., and Antonov, J.: Climatological
642 annual cycle of upper ocean oxygen content anomaly, *Geophys. Res. Lett.*, 32, L05611,
643 <https://doi.org/10.1029/2004GL021745>, 2005.
644

645 Garcia, H. E., Weathers, K., Paver, C. R., Smolyar, I., Boyer, T. P., Locarnini, R. A., Zweng,
646 M. M., Mishonov, A. V., Baranova, O. K., Seidov, D., and Reagan, J. R.: *World Ocean
647 Atlas 2018, Volume 3: Dissolved Oxygen, Apparent Oxygen Utilization, and Oxygen
648 Saturation*, A. Mishonov Technical Ed., NOAA Atlas NESDIS 83, 2018.
649

650 Garcia, H. E., Wang, Z., Bouchard, C., Cross, S. L., Paver, C. R., Reagan, J. R., Boyer, T. P.,
651 Locarnini, R. A., Mishonov, A. V., Baranova, O. K., Seidov, D., and Dukhovskoy, D.:
652 *World Ocean Atlas 2023, Volume 3: Dissolved Oxygen, Apparent Oxygen Utilization,
653 Dissolved Oxygen Saturation, and 30-year Climate Normal*, A. Mishonov Technical
654 Editor, NOAA Atlas NESDIS 91, 100 pp., <https://doi.org/10.25923/rb67-ns53>, 2024.
655

656 Garcia-Soto, C., Cheng, L., Caesar, L., Schmidtko, S., Jewett, E. B., Cheripka, A., Rigor, I.,
657 Caballero, A., Chiba, S., Báez, J. C., Zielinski, T., and Abraham, J. P.: An Overview of
658 Ocean Climate Change Indicators: Sea Surface Temperature, Ocean Heat Content,
659 Ocean pH, Dissolved Oxygen Concentration, Arctic Sea Ice Extent, Thickness and
660 Volume, Sea Level and Strength of the AMOC (Atlantic Meridional Overturning
661 Circulation), *Front. Mar. Sci.*, 8, 642372, <https://doi.org/10.3389/fmars.2021.642372>,
662 2021.
663

664 Gouretski, V., Cheng, L., Du, J., Xing, X., and Chai, F.: A quality-controlled and bias-
665 adjusted global ocean oxygen profile dataset, *Marine Science Data Center of the Chinese
666 Academy of Sciences*, <http://dx.doi.org/10.12157/IOCAS.20231208.001>, 2024.
667

668 Gouretski, V., Cheng, L., Du, J., Xing, X., Chai, F., and Tan, Z.: A consistent ocean oxygen
669 profile dataset with new quality control and bias assessment, *Earth Syst. Sci. Data*, 16,
670 5503-5530, <https://doi.org/10.5194/essd-16-5503-2024>, 2024.
671

672 Gregoire, M., Garçon, V., Garcia, H., Oschlies, A., Schmidtko, S., Isensee, K., et al.: A
673 Global Ocean Oxygen Database and Atlas for Assessing and Predicting Deoxygenation
674 and Ocean Health in the Open and Coastal Ocean, *Front. Mar. Sci.*, 8, 1-29,
675 <https://doi.org/10.3389/fmars.2021.724913>, 2021.
676

677 Gulev, S. K., Thorne, P. W., Ahn, J., Dentener, F. J., Domingues, C. M., Gerland, S., Gong,
678 D., Kaufman, D. S., Nnamchi, H. C., Quaas, J., Rivera, J. A., Sathyendranath, S. L.,
679 Smith, S. L., Trewin, B., von Schuckmann, K., and Vose, R. S.: Changing State of the
680 Climate System, In: *Climate Change 2021: The Physical Science Basis. Contribution of*
681 *Working Group I to the Sixth Assessment Report of the Intergovernmental Panel on*
682 *Climate Change*, edited by: Masson-Delmotte, V., Zhai, P., Pirani, A., Connors, S. L.,
683 Péan, C., Berger, S., Caud, N., Chen, Y., Goldfarb, L., Gomis, M. I., Huang, M., Leitzell,
684 K., Lonnoy, E., Matthews, J. B. R., Maycock, T. K., Waterfield, T., Yelekçi, O., Yu, R.,
685 and Zhou, B., Cambridge University Press, Cambridge, United Kingdom and New York,
686 NY, USA, 287-422, <https://doi.org/10.1017/9781009157896.004>, 2021.

687

688 Huang, S., Shao, J., Chen, Y., Qi, J., Wu, S., Zhang, F., He, X., and Du, Z.: Reconstruction of
689 dissolved oxygen in the Indian Ocean from 1980 to 2019 based on machine learning
690 techniques, *Front. Mar. Sci.*, 10, 1291232, <https://doi.org/10.3389/fmars.2023.1291232>,
691 2023.

692

693 IOC, SCOR, and IAPSO: The International thermodynamic equation of seawater-2010:
694 Calculation and use of thermodynamic properties, Intergovernmental Oceanographic
695 Commission, Manuals and Guides No. 56, UNESCO, 2010.

696

697 Ito, T., Minobe, S., Long, M. C., and Deutsch, C.: Upper ocean O₂ trends: 1958-2015,
698 *Geophys. Res. Lett.*, 44, 4214-4223, <https://doi.org/10.1029/2017GL073613>, 2017.

699

700 Ito, T., Cervania, A., Cross, K., Ainchwar, S., and Delawalla, S.: Mapping dissolved oxygen
701 concentrations by combining shipboard and Argo observations using machine learning
702 algorithms, *J. Geophys. Res.-Mach. Learn. Comput.*, 1, e2024JH000272,
703 <https://doi.org/10.1029/2024JH000272>, 2024.

704

705 Ito, T., Garcia, H. E., Wang, Z., Cheng, L., Du, J., Roach, C. J., Sharp, J. D., Minobe, S.,
706 Zhou, Y., Lu, B., Navarra, G. G., and Bushinsky, S. M.: Assessing the observational
707 uncertainties of dissolved oxygen climatology and seasonal cycle through a coordinated
708 intercomparison project, *Global Biogeochem. Cy.*, 39, e2025GB008751,
709 <https://doi.org/10.1029/2025GB008751>, 2025.

710

711 Keeling, R. F., Körtzinger, A., and Gruber, N.: Ocean Deoxygenation in a Warming world,
712 *Annu. Rev. Mar. Sci.*, 2, 199-229,
713 <https://doi.org/10.1146/annurev.marine.010908.163855>, 2010.

714

715 Koelling, J., Atamanchuk, D., Karstensen, J., Handmann, P., and Wallace, D. W. R.: Oxygen
716 export to the deep ocean following Labrador Sea Water formation, *Biogeosciences*, 19,
717 437-454, <https://doi.org/10.5194/bg-19-437-2022>, 2022.

718

719 Kwiecinski, J. V., and Babbitt, A. R.: A high-resolution atlas of the eastern tropical Pacific
720 oxygen deficient zones, *Global Biogeochem. Cy.*, 35, e2021GB007001,
721 <https://doi.org/10.1029/2021GB007001>, 2021.

722

723 Lauvset, S. K., Key, R. M., Olsen, A., van Heuven, S., Velo, A., Lin, X., Schirnick, C.,
724 Kozyr, A., Tanhua, T., Hoppema, M., Jutterström, S., Steinfeldt, R., Jeansson, E., Ishii,
725 M., Perez, F. F., Suzuki, T., and Watelet, S.: A new global interior ocean mapped

726 climatology: the $1^{\circ} \times 1^{\circ}$ GLODAP version 2, *Earth Syst. Sci. Data*, 8, 325-340,
727 <https://doi.org/10.5194/essd-8-325-2016>, 2016.
728

729 Levin, L. A.: Manifestation, drivers, and emergence of open ocean deoxygenation, *Annu.*
730 *Rev. Mar. Sci.*, 10, 229-260, <https://doi.org/10.1146/annurev-marine-121916-063359>,
731 2018.
732

733 Liu, Q. H., Bao, S. L., Yan, H. Q., Wang, H. Z., and Zhang, R.: Enhancing sea surface
734 salinity short-term prediction using physically informed deep learning, *Appl. Ocean*
735 *Res.*, 165, 104832, <https://doi.org/10.1016/j.apor.2025.104832>, 2025.
736

737 Lu, B., Zhao, Z., Han, L. Y., Gan, X. Y., Zhou, Y. T., Zhou, L., Fu, L. Y., Wang, X. B.,
738 Zhou, C. H., and Zhang, J.: A Spatio-Temporal Graph Hypernetwork for Reconstruction
739 of Global Ocean Dissolved Oxygen, *Proceedings of the 41st International Conference on*
740 *Machine Learning*, Vienna, Austria, PMLR 235, 2024.
741

742 Martin, A.P.: The seasonal smorgasbord of the seas, *Science*, 337(6090), 46-47,
743 <https://doi.org/10.1126/science.1223881>, 2012.
744

745 McDougall, T. J., and Barker, P. M.: Getting started with TEOS-10 and the Gibbs Seawater
746 (GSW) oceanographic toolbox, *SCOR/IAPSO WG127*, 1-28, 2011.
747

748 Mishonov, A. V., Boyer, T. P., Baranova, O. K., Bouchard, C., Cross, S. L., Garcia, H. E.,
749 Locarnini, R. A., Paver, C. R., Reagan, J. R., Wang, Z., Seidov, D., Grodsky, A. I., and
750 Beauchamp, J. G.: *World Ocean Database 2023*, C. Bouchard, Technical Ed., NOAA
751 Atlas NESDIS 97, <https://doi.org/10.25923/z885-h264>, 2024.
752

753 Musan, I., Gildor, H., Barkan, E., Smethie, W. M., Jr., and Luz, B.: Evidence from dissolved
754 O₂ isotopes in North Atlantic Deep Water for a recent climatic shift, *Geophys. Res.*
755 *Lett.*, 50, e2022GL100489, <https://doi.org/10.1029/2022GL100489>, 2023.
756

757 Oschlies, A., Duteil, O., Getzlaff, J., Koeve, W., Landolfi, A., and Schmidtko, S.: Patterns of
758 deoxygenation: sensitivity to natural and anthropogenic drivers, *Philos. T. R. Soc. A*,
759 375, 20160325, <https://doi.org/10.1098/rsta.2016.0325>, 2017.
760

761 Oschlies, A., Brandt, P., Stramma, L., and Schmidtko, S.: Drivers and mechanisms of ocean
762 deoxygenation, *Nat. Geosci.*, 11, 467-473, <https://doi.org/10.1038/s41561-018-0152-2>,
763 2018.
764

765 Roach, C. J., and Bindoff, N. L.: Developing a New Oxygen Atlas of the World's Oceans
766 Using Data Interpolating Variational Analysis, *J. Atmos. Ocean. Tech.*, 40, 1475-1491,
767 <https://doi.org/10.1175/JTECH-D-23-0007.1>, 2023.
768

769 Ruhl, H. A., Huffard, C. L., Messié, M., Connolly, T. P., Soltwedel, T., Wenzhöfer, F.,
770 Wallace, D. W. R., et al.: Decadal change in deep-ocean dissolved oxygen in the North
771 Atlantic Ocean and North Pacific Ocean, *Deep-Sea Res. Pt. I*, 223, 104534,
772 <https://doi.org/10.1016/j.dsr.2025.104534>, 2025.
773

774 Schmidtko, S., Stramma, L., and Visbeck, M.: Decline in global oceanic oxygen content
775 during the past five decades, *Nature*, 542, 335-339, <https://doi.org/10.1038/nature21399>,
776 2017.
777

778 Sharp, J. D., Fassbender, A. J., Carter, B. R., Johnson, G. C., Schultz, C., and Dunne, J. P.:
779 GOBAI-O2: temporally and spatially resolved fields of ocean interior dissolved oxygen
780 over nearly 2 decades, *Earth Syst. Sci. Data*, 15, 4481-4518,
781 <https://doi.org/10.5194/essd-15-4481-2023>, 2023.
782

783 Stramma, L., Johnson, G. C., Sprintall, J., and Mohrholz, V.: Expanding oxygen-minimum
784 zones in the tropical oceans, *Science*, 320, 655-658,
785 <https://doi.org/10.1126/science.1153847>, 2008.
786

787 Stramma, L., and Schmidtko, S.: Spatial and temporal variability of oceanic oxygen changes
788 and underlying trends, *Atmos.-Ocean*, 59, 122-132,
789 <https://doi.org/10.1080/07055900.2021.1905601>, 2021.
790

791 Tan, Z., Schuckmann, K. v., Speich, S., Bopp, L., Zhu, J., and Cheng, L.: Observed large-
792 scale and deep-reaching compound ocean state changes over the past 60 years. *Nat.*
793 *Clim. Chang*, 16, 58–68, <https://doi.org/10.1038/s41558-025-02484-x>, 2026.
794

795 Wang, Z., Garcia, H. E., Boyer, T. P., Reagan, J., and Cebrian, J.: Controlling factors of the
796 climatological annual cycle of the surface mixed layer oxygen content: A global view,
797 *Front. Mar. Sci.*, 9, 1001095, <https://doi.org/10.3389/fmars.2022.1001095>, 2022.
798

799 Whitney, F. A., Bograd, S. J., and Ono, T.: Nutrient enrichment of the subarctic Pacific
800 Ocean pycnocline, *Geophys. Res. Lett.*, 40, 2200-2205,
801 <https://doi.org/10.1002/grl.50439>, 2013.
802

803 Zhou, Y., Gong, H., and Zhou, F.: Responses of horizontally expanding oceanic oxygen
804 minimum zones to climate change based on observations, *Geophys. Res. Lett.*, 49,
805 e2022GL097724, <https://doi.org/10.1029/2022GL097724>, 2022.
806
807